

Dispersive-optical-model analysis of the asymmetry dependence of correlations in Ca isotopesR. J. Charity,¹ J. M. Mueller,² L. G. Sobotka,^{1,2} and W. H. Dickhoff²¹*Department of Chemistry, Washington University, St. Louis, Missouri 63130, USA*²*Department of Physics, Washington University, St. Louis, Missouri 63130, USA*

(Received 1 August 2007; published 18 October 2007)

A dispersive-optical-model analysis of $p+^{40,42,44,48}\text{Ca}$ and $n+^{40}\text{Ca}$ interactions has been carried out. The real and imaginary potentials have been constrained by fitting elastic-scattering data, total and reaction cross sections, and level properties of valence hole states deduced from $(e, e'p)$ data. The resulting surface imaginary potential increases with asymmetry for protons, implying that in heavier Ca isotopes, protons experience stronger long-range correlations. Presently, there is not enough data for neutrons to determine their asymmetry dependence. Global optical-model fits usually assume that the neutron asymmetry dependence is equal in magnitude, but opposite in sign, to that for protons. Such a dependence was found to give unphysical results for heavy Ca isotopes. The dispersive optical model is shown to be a useful tool for data-driven extrapolations to the drip lines. Neutron and proton data at larger asymmetries are needed to achieve more reliable extrapolations. The present analysis predicts ^{60}Ca and ^{70}Ca to be bound, while the intermediate isotopes are not.

DOI: [10.1103/PhysRevC.76.044314](https://doi.org/10.1103/PhysRevC.76.044314)

PACS number(s): 24.10.Ht, 11.55.Fv, 21.10.Pc, 27.50.+e

I. INTRODUCTION

A full understanding of nuclear properties requires knowledge of the correlations between the nucleons. These correlations cause the spectroscopic strength of single-particle levels to be reduced relative to independent-particle-model (IPM) values. Furthermore, the strength is spread in energy; and for stable closed-shell nuclei, the spectroscopic factors measured in $(e, e'p)$ reactions are about 65% of the IPM predictions. The theoretical interpretation [1] of these observations points to a global depletion of the shell-model Fermi sea due to short-range correlations accompanied by a complementary presence of high-momentum components that have recently been observed [2]. A quantitative understanding of the spectroscopic factors obtained from the $(e, e'p)$ reaction requires a substantial contribution from long-range correlations that represent the coupling of the single-particle states to low-lying collective excitations that are dominated by surface properties of the nucleus. With an increasing interest in nuclei far from stability, it is important to understand how these correlations are modified as one approaches the drip lines. Nuclear-matter calculations suggest that protons (neutrons) feel stronger (weaker) correlations with increasing neutron fraction [3]. These effects are related to the increased (decreased) importance of the stronger p - n tensor interaction compared to the p - p (n - n) interaction for protons (neutrons) with increasing asymmetry. In addition to these volume effects associated with short-range and tensor correlations, one must consider the long-range correlations associated with the coupling of surface excitations, which are present in finite nuclei, to single-particle degrees of freedom. The asymmetry $(N - Z)/A$ dependence of these latter correlations has not been well studied.

Experimentally, spectroscopic factors for hole states measured in knockout reactions provide evidence for an asymmetry dependence. Gade *et al.* [4] have observed that the reduction factor, the ratio of the measured spectroscopic factor relative to the shell-model value, decreases strongly with nucleon

separation energy. The latter, of course, is related to the asymmetry.

An appropriate framework for studying correlations is to constrain the nucleon self-energy $\Sigma(rm, r'm'; E)$. With knowledge of this complex, energy-dependent, nonlocal and spin-dependent quantity, the Dyson equation can be solved, thereby generating the nucleon single-particle propagator [5]. From this propagator, one can calculate all single-particle properties pertaining to the ground state of the system, such as spectroscopic factors and occupation numbers (in any basis), the charge and matter distributions, and the contribution to the energy of the ground state from two-body interaction terms. The standard optical-model (OM) potential for nucleon elastic scattering represents a local approximation of this self-energy for positive energies. The imaginary OM potential is usually decomposed into surface and volume components. The surface contribution, which is dominant at small positive energies, accounts mostly for long-range correlations associated with couplings to low-lying collective states and giant resonances. At higher energies, the volume contribution dominates and is associated with short-range correlations that can be conveniently studied theoretically in nuclear matter.

Mahaux and Sartor [6] developed the dispersive optical model (DOM) to extend the OM potential down to negative energies, and thus the DOM can address bound single-particle properties as well as elastic nucleon scattering. There are a number of examples of DOM fits to proton and neutron elastic-scattering data [7–15]. Fitted DOM potentials usually describe single-particle properties reasonably well.

Parametrized OM potentials derived from global fits to nucleon elastic-scattering data, such as the Becchetti and Greenlees [16] and the Chapel Hill 89 [17] versions, include an asymmetry dependence. The asymmetry dependence of the real potential is related to the symmetry energy. Of more importance in the present study is the asymmetry dependence of the imaginary potential that when implemented in the DOM, results in an asymmetry dependence of occupation probabilities, spectroscopic factors, and other

quantities related to correlations. In the OM fits, the asymmetry dependence of the imaginary potential is attributed solely to the surface component associated with long-range correlations. The volume component, associated more with short-range correlations is asymmetry independent. These fits suggest that the long-range correlations associated with coupling to low-lying collective excitations and giant resonances have the largest asymmetry dependence.

This paper reports on a continuation of a DOM analysis of scattering and bound-state data for Ca isotopes. In Ref. [18], DOM fits of $p+^{40}\text{Ca}$ and $p+^{48}\text{Ca}$ data indicated that protons are more strongly correlated in the neutron-rich ^{48}Ca nucleus. The present work extends this analysis by adding the $p+^{42}\text{Ca}$, $p+^{44}\text{Ca}$, and $n+^{40}\text{Ca}$ systems to this analysis. In addition, the data sets for the $p+^{40}\text{Ca}$ and $p+^{48}\text{Ca}$ systems were buttressed with more elastic-scattering data now including proton energies up to 200 MeV.

To extrapolate the results to nuclei near the drip lines, it is imperative that one determine the asymmetry dependence of the imaginary part of the DOM potential. Following our previous study and the global OM fits, the asymmetry dependence will be confined to the surface imaginary potential. We will ignore the volume component which appears to have a weaker asymmetry dependence. In any case, we are compelled to do so, as there are still not sufficient data at high energies for $N \neq Z$ targets to adequately constrain its dependence [18]. The asymmetry dependence of the surface component is well determined from the experimental data for protons. We will consider two possible asymmetry dependences for neutrons and their consequences.

A brief description of the DOM is given in Sec. II, while the data sets used in the DOM fits are listed in Sec. III. Information about integrated OM potentials is presented in Sec. IV. The parametrizations of the real and imaginary potentials are given in Sec. V, while the results of the fit are given in Sec. VI. The implication of the fitted potentials for correlations are presented in Sec. VII. Finally, Sec. VIII lists the conclusions of this study.

II. DISPERSIVE OPTICAL MODEL

The optical-model potential is related to the nucleon self-energy $\Sigma(\mathbf{r}m, \mathbf{r}'m'; E)$ which is complex, nonlocal, spin, isospin, and energy dependent. Once this self-energy is specified, the Dyson equation can be solved yielding the single-particle properties of the system under study. In the DOM, the optical-model potential is a local approximation to $\Sigma(\mathbf{r}m, \mathbf{r}'m'; E)$ representing the traditional analysis of nucleon scattering and bound single-particle properties. This section gives a brief description of the derivation of the DOM and the calculation of bound-state properties. Additional details can be found in Ref. [6].

In deriving the DOM potential, Mahaux and Sartor [6] start with the real part of the nucleon self-energy, which can be written as

$$\text{Re } \Sigma(\mathbf{r}, \mathbf{r}'; E) = \text{Re } \Sigma(\mathbf{r}, \mathbf{r}'; E_F) + \Delta\mathcal{V}(\mathbf{r}, \mathbf{r}'; E), \quad (1)$$

where E_F is the Fermi energy and (iso)spin indices have been suppressed for notational convenience. Here the first term is the static or energy-independent part, and the second term $\Delta\mathcal{V}$, the dispersive correction, contains the energy dependence. This term can be obtained from the imaginary part of the self-energy through a subtracted dispersion relation

$$\Delta\mathcal{V}(\mathbf{r}, \mathbf{r}'; E) = +\frac{1}{\pi} P \int \text{Im } \Sigma(\mathbf{r}, \mathbf{r}'; E') \times \left(\frac{1}{E' - E} - \frac{1}{E' - E_F} \right) dE', \quad (2)$$

where P stands for the principal value. The dispersion relation is a consequence of causality, and a subtracted form is used here so that $\Delta\mathcal{V}(\mathbf{r}, \mathbf{r}'; E_F) = 0$. The dispersive correction varies rapidly around E_F and causes the valence single-particle levels to be focused toward the Fermi energy.

The effect of a nonlocal real potential can be approximately represented by an energy-dependent local potential [19]. While this procedure allows one to make contact with a considerable amount of experience in describing nuclear properties, it is necessary to adhere to the nonlocal form for a complete solution of the Dyson equation that yields the relevant single-particle properties of the ground state, such as the charge density. In the present paper, we continue to employ an energy-dependent optical-model potential $\mathcal{U}(r, E) = \mathcal{V}(r, E) + i\mathcal{W}(r, E)$ as a local approximation to the nucleon self-energy. Equation (1) then becomes

$$\mathcal{V}(r, E) = \mathcal{V}_{\text{HF}}(r, E) + \Delta\mathcal{V}(r, E), \quad (3)$$

and the corresponding local dispersive correction is given by

$$\Delta\mathcal{V}(r, E) = \frac{1}{\pi} P \int \mathcal{W}(r, E') \left(\frac{1}{E' - E} - \frac{1}{E' - E_F} \right) dE'. \quad (4)$$

In Eq. (3), $\mathcal{V}_{\text{HF}}(r, E)$ is the local equivalent of $\text{Re } \Sigma(\mathbf{r}, \mathbf{r}'; E_F)$. It contains the nonlocal effects that are contained in Hartree-Fock calculations with phenomenological effective interactions and hence is called the Hartree-Fock potential by Mahaux and Sartor, but it should not be confused with the Hartree-Fock self-energy contribution of a realistic nucleon-nucleon interaction.

The energy derivative of \mathcal{V}_{HF} is a measure of nonlocality, which is related to the momentum-dependent effective mass

$$\frac{\tilde{m}(r, E)}{m} = 1 - \frac{d\mathcal{V}_{\text{HF}}(r, E)}{dE}, \quad (5)$$

where m is the nucleon mass. The Hartree-Fock potential is expected to have a smooth energy dependence compared to the more rapid dependence of the dispersive correction. One well-known consequence of the replacement of $\text{Re } \Sigma(\mathbf{r}, \mathbf{r}'; E_F)$ by $\mathcal{V}_{\text{HF}}(r, E)$ is that wave functions obtained with the local potential must be scaled by the factor $\sqrt{\tilde{m}(r, E)/m}$ to fully account for nonlocality [19]. In addition, this treatment requires one to scale $\text{Im } \Sigma(\mathbf{r}, \mathbf{r}'; E')$, and thus $\Delta\mathcal{V}(\mathbf{r}, \mathbf{r}'; E)$ by $\tilde{m}(r, E)/m$ [6]. The imaginary potential in Eq. (4) is also replaced by a local equivalent. Mahaux and Sartor argue that this change modifies $\Delta\mathcal{V}$ by a smooth function of energy,

which can be compensated by a correspondingly smooth change in the energy dependence of \mathcal{V}_{HF} .

In addition to the momentum-dependent effective mass, two other effective masses can be defined. The total effective mass is given by

$$\frac{m^*(r, E)}{m} = 1 - \frac{d\mathcal{V}(r, E)}{dE}, \quad (6)$$

while the energy-dependent effective mass is

$$\frac{\bar{m}(r, E)}{m} = 1 - \frac{m}{\tilde{m}(r, E)} \frac{d\Delta\mathcal{V}(r, E)}{dE}. \quad (7)$$

At the highest energies considered in this work, relativistic effects become relevant. We have included a corresponding lowest order correction in solving the radial wave equation [20]

$$\left[\frac{d^2}{d\rho^2} + \left(1 - \frac{\tilde{U}(\rho, E)}{E_{\text{tot}} - M - m} - \frac{\ell(\ell + 1)}{\rho^2} \right) \right] u(\rho) = 0, \quad (8)$$

with $\rho = kr$, where $k = \frac{M}{E_{\text{tot}}} \sqrt{T(T + 2m)}$, T is the laboratory kinetic energy, E_{tot} is the total energy in the center-of-mass frame, and M is the target mass. The scaled potential is

$$\tilde{U} = \gamma \mathcal{U}, \quad \gamma = \frac{2(E_{\text{tot}} - M)}{E_{\text{tot}} - M - m}. \quad (9)$$

If $u_{n\ell j}(r)$ are bound-state solutions to the radial wave equation, then the normalized wave functions corrected for nonlocality are given by

$$\bar{u}_{n\ell j}(r) = \sqrt{\frac{\tilde{m}(r, E_{n\ell j})}{m}} u_{n\ell j}(r). \quad (10)$$

In this work, we have employed the following approximations, developed by Mahaux and Sartor [6], to determine bound-state properties. The width of a state is given by

$$\Gamma_{n\ell j} = -2 \frac{\int_0^\infty \bar{u}_{n\ell j}^2(r) \mathcal{W}(r, E_{n\ell j}) dr}{\int_0^\infty \bar{u}_{n\ell j}^2(r) \frac{m^*(r, E_{n\ell j})}{m} dr}, \quad (11)$$

where the spectroscopic factor for valence states is

$$S_{n\ell j} = \int_0^\infty \bar{u}_{n\ell j}^2(r) \frac{m}{\bar{m}(r, E_{n\ell j})} dr, \quad (12)$$

with root-mean-square (rms) radius of

$$R_{\text{rms}}^{n\ell j} = \sqrt{\int_0^\infty \bar{u}_{n\ell j}^2(r) r^2 dr}. \quad (13)$$

For hole states, the occupation probability is approximated by

$$N_{n\ell j} = \int_0^\infty \bar{u}_{n\ell j}^2(r) \left[1 + \frac{m}{\bar{m}(r, E_{n\ell j})} \times \frac{P}{\pi} \int_{E_F}^\infty \frac{\mathcal{W}(r, E')}{(E' - E_{n\ell j})^2} dE' \right] dr, \quad (14)$$

while for particle states, the same approximation gives

$$N_{n\ell j} = - \int_0^\infty \bar{u}_{n\ell j}^2(r) \left[\frac{m}{\bar{m}(r, E_{n\ell j})} \times \frac{P}{\pi} \int_{-\infty}^{E_F} \frac{\mathcal{W}(r, E')}{(E' - E_{n\ell j})^2} dE' \right] dr. \quad (15)$$

TABLE I. Elastic scattering data for $p+^{40}\text{Ca}$ reactions used in the fits.

E (MeV)	$\frac{d\sigma}{d\Omega}$	A_y	Q	Ref.
17.57	x			[42]
19.57	x			[43]
21.0	x	x		[44,45]
25.0	x			[45]
26.3	x	x		[45,46]
30.0	x			[45]
30.3		x		[47]
35.0	x			[45]
40.0	x	x		[45,48]
45.0	x			[45]
48.0	x			[45]
49.0		x		[49]
61.4	x			[50]
65.0	x	x	x	[23,51]
80.2	x	x		[20,52]
100.6	x	x		[53]
135.1	x			[20]
152.0	x			[54]
160.0	x	x		[20,52]
181.0	x	x		[20,52]
200.0	x	x	x	[22]

III. DATA SETS

The optical-model potential is constrained using a large number of published data sets at both positive and negative energies. These include the following data sets:

- (i) Elastic-scattering angular distributions $d\sigma/d\Omega$ and analyzing powers A_y for $p+^{40,42,44,48}\text{Ca}$ and $n+^{40}\text{Ca}$ with energies up to 200 MeV. The energies and references for these data are listed in Tables I–V. Only the $p+^{40}\text{Ca}$ data are significant and constraining at the higher energies where the volume absorption is dominant. Spin rotation parameters Q [21] are available for 200 MeV $p+^{40,48}\text{Ca}$ [22] and 65 MeV $p+^{40}\text{Ca}$ [23]. These were not used in the fits but are compared with the final DOM predictions.
- (ii) Reaction cross sections σ_{react} for $p+^{40,42,44,48}\text{Ca}$ reactions from Ref. [24] and for the $n+^{40}\text{Ca}$ reaction from

TABLE II. Elastic scattering data for $p+^{42}\text{Ca}$ reactions used in the fits.

E (MeV)	$\frac{d\sigma}{d\Omega}$	A_y	Ref.
21.0	x		[45]
25.0	x		[45]
30.0	x		[45]
35.0	x		[45]
40.0	x		[45]
45.0	x		[45]
48.4	x		[45]
65.0	x	x	[51]

TABLE III. Elastic scattering data for $p+^{44}\text{Ca}$ reactions used in the fits.

E (MeV)	$\frac{d\sigma}{d\Omega}$	A_y	Ref.
21.0	x		[45]
25.0	x		[45]
30.0	x		[45]
40.0	x		[45]
45.0	x		[45]
48.4	x		[45]
65.0	x	x	[51]

Ref. [25]. Again, only for the $p+^{40}\text{Ca}$ reaction are there data above 50 MeV.

- (iii) Total reaction cross sections σ_{total} for the $n+^{40}\text{Ca}$ reaction at energies from 8 to 200 MeV [26–29]. Comparisons were made to σ_{total} data for the $n+^{44}\text{Ca}$ reaction [30], but these were not included in the fit.
- (iv) Single-particle energies for proton and neutron levels from Refs. [31–37].
- (v) For the $0d_{5/2}$, $1s_{1/2}$, and $0d_{3/2}$ proton holes states in ^{40}Ca and ^{48}Ca , the widths Γ , rms radii R_{rms} , and spectroscopic factors S measured in the $(e, e'p)$ reactions at the National Instituut voor Kernfysica en Hoge-Energiefysica, Netherlands (NIKHEF) by Kramer *et al.* [38,39]. The spectroscopic factor for the $1s_{1/2}$ state in ^{40}Ca , although shown in subsequent plots, was not included in the fits. More recent experiments by the same group indicate that the value of this quantity is larger than the published value [40].
- (vi) Experimental widths of the neutron holes states in ^{40}Ca measured in $^{40}\text{Ca}(p, d)^{39}\text{Ca}$ transfer reactions [36] were not used in the DOM fits but were compared with final DOM predictions.

TABLE IV. Elastic scattering data for $p+^{48}\text{Ca}$ reactions used in the fits.

E (MeV)	$\frac{d\sigma}{d\Omega}$	A_y	Q	Ref.
8.0	x	x		[55]
10.0	x	x		[55]
12.0	x	x		[55]
14.03	x	x		[56]
15.05	x	x		[56]
15.65	x	x		[56]
21.0	x			[45]
25.0	x			[45]
30.0	x			[45]
35.0	x			[45]
40.0	x			[45]
45.0	x			[45]
48.4	x			[45]
65.0	x	x		[51]
200.0	x	x	x	[22]

TABLE V. Elastic scattering data for $n+^{40}\text{Ca}$ reactions used in the fits.

E (MeV)	$\frac{d\sigma}{d\Omega}$	A_y	Ref.
9.9	x	x	[57]
11.0	x		[58]
11.9	x	x	[57]
13.9	x	x	[57,59]
16.9	x	x	[59]
19.0	x		[60]
20.0	x		[58]
21.7	x		[60]
25.5	x		[60]
26.0	x		[58]
30.0	x		[61]
40.0	x		[61]
65.0	x		[62]
75.0	x		[62]
85.0	x		[62]
95.0	x		[62]
107.5	x		[62]
127.5	x		[62]
155.0	x		[62]
185.0	x		[62]

- (vii) Fermi energies determined from experimental masses M following Ref. [41], i.e.,

$$E_F = \frac{E_F^+ + E_F^-}{2}, \quad (16)$$

$$E_F^+ = M_{A+1} - M_A - m, \quad (17)$$

$$E_F^- = M_A - M_{A-1} - m, \quad (18)$$

where m is either the proton or neutron mass and E_F^- and E_F^+ are the separation energies of the A and $A+1$ nucleon systems.

IV. INTEGRATED POTENTIALS

Ambiguities in determining potentials in standard OM fits are well known; however, volume integrals and rms radii of potentials are known to be better defined [6,63]. The volume integral and rms radius of the real potential \mathcal{V} are given by

$$J_V = \int \mathcal{V}(r) dr, \quad (19)$$

$$R_{\text{rms}}^V = \sqrt{\frac{\int r^2 \mathcal{V}(r) dr}{J_V}}. \quad (20)$$

Similar quantities for the imaginary J_W , R_{rms}^W and spin-orbit terms J_{so} , $R_{\text{rms}}^{\text{so}}$ can be defined. Mahaux and Sartor used such quantities to constrain the DOM potential [6]. Although we fit the experimental data directly, these quantities proved useful in choosing the parametrization of the various potentials.

As an example, the asymmetry dependence of $|J_W/A|$ is shown in Fig. 1 at four energies. These data points were

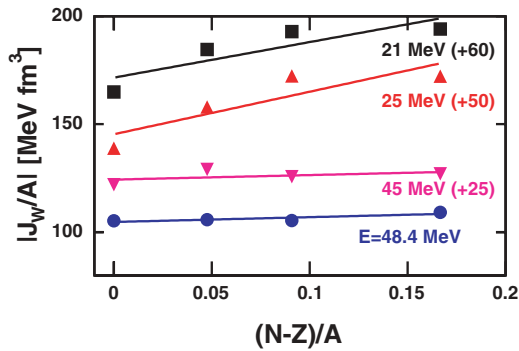


FIG. 1. (Color online) Asymmetry dependence of the integrated imaginary potential. Data points are from the optical-model fits of Ref. [45]. Lines are linear-least-square fits to these points. The lines and data have been offset along the y axis by the indicated amounts.

obtained from optical-model fits by McCamis *et al.* to their measured $p+^{40,42,44,48}\text{Ca}$ elastic-scattering angular distributions [45]. For the lowest two energies ($E = 21, 25$ MeV), there is a clear asymmetry dependence of J_W . However, at $E = 45$ and 48.4 MeV, this dependence has largely disappeared. The asymmetry dependence of J_W therefore appears to be confined to low energies where surface absorption is dominant. These observations are consistent with global optical-model fits which require an asymmetry dependence of the surface term W_s , but not for the volume contribution W_v [16,17]. From all published OM fits, the dependence of $|J_W/A|$ on $E - E_F$ is plotted in Fig. 2 for the $p+^{40}\text{Ca}$, $n+^{40}\text{Ca}$, and $p+^{48}\text{Ca}$ reactions. The fluctuations of J_W are expected to be larger in this figure as the different studies are not consistent in the parametrizations of the potentials, and the quality of the fits varies from study to study. As best one can tell, the energy dependence for proton and neutron scattering on ^{40}Ca are identical. However for $p+^{48}\text{Ca}$, the

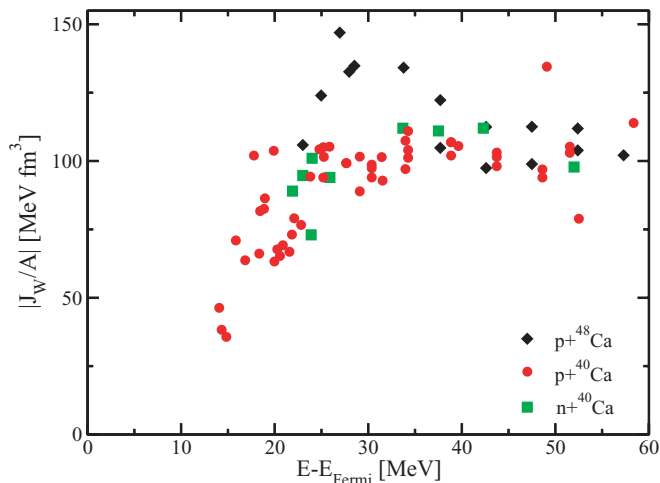


FIG. 2. (Color online) Energy dependence of the integrated imaginary potential determined from published optical-model fits to $p+^{40}\text{Ca}$, $p+^{48}\text{Ca}$, and $n+^{48}\text{Ca}$ elastic-scattering data.

$|J_W/A|$ values are consistently higher than for $p+^{40}\text{Ca}$ in the energy regime $E - E_F < 40$ MeV and relax toward these values for higher energies. These results again indicate that the surface imaginary component has the largest asymmetry dependence and justifies our assumption that the asymmetry dependence of the volume term can be ignored as a first approximation.

The energy dependence of the potentials at higher energies are determined mainly by the $p+^{40}\text{Ca}$ and $n+^{40}\text{Ca}$ data. To further constrain the integrated potentials and rms radii in this region, combined fits to the $p+^{40}\text{Ca}$ elastic-scattering data and $n+^{40}\text{Ca}$ total cross sections were made. Neutron and proton potentials for a symmetric system like ^{40}Ca are expected to be identical once the proton energy is corrected for the Coulomb potential. In this work, the Coulomb correction is given by the difference between the proton and neutron Fermi energies ($E_c = 7.20$ MeV). This can be compared favorably to the value of $E_c = 7.95$ MeV from the global OM parametrization of Varner *et al.* [17]. Proton elastic-scattering data sets in Table I containing both angular-distribution and analyzing-power information were fit with a standard OM simultaneously with the neutron total cross section interpolated from Refs. [26–29] at an energy consistent with the Coulomb correction. The integrated potentials and rms radii obtained from these fits are plotted as a function of $E - E_F$ in Fig. 3. The inclusion of the neutron cross sections in the fits reduced the fluctuations in all of these quantities, especially for the rms radii.

A number of important trends are observed in these data. First, the spin-orbit term J_{so} is approximately constant but shows a small, but significant, decrease with energy. Second, for the imaginary potential, R_{rms}^W continues to decrease above $E - E_F = 50$ MeV, where the asymmetry dependence has largely vanished. It is possible that the radial dependence of the volume term W_v is itself energy dependent or that there is an asymmetry-independent surface component that persists to larger energies. These two possibilities are indistinguishable in practice, since adding a small surface correction to a volume component is equivalent to modifying the radius of the volume component. Finally for the real potential, R_{rms}^V shows much less

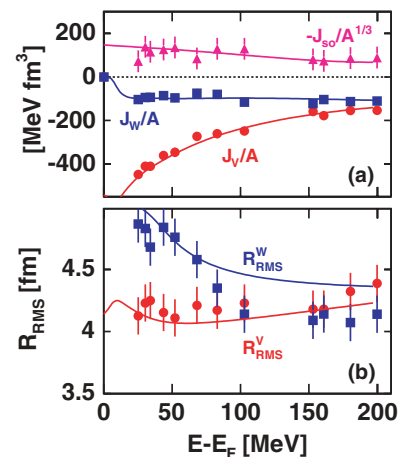


FIG. 3. (Color online) (a) Integrated potentials and (b) rms radii obtained from combined fits to $p+^{40}\text{Ca}$ elastic-scattering data and $n+^{40}\text{Ca}$ total cross sections.

energy dependence and may increase at the highest energies. The latter may be an indication of a “wine-bottle”-shaped potential (see Sec. V).

V. PARAMETRIZATION OF THE POTENTIALS

The imaginary potential is composed of the sum of the volume, surface, and imaginary spin-orbit components,

$$\mathcal{W}(r, E) = -W_v(E)f(r, r_v, a_v) + 4a_s W_s(E) \frac{d}{dr} f(r, r_s, a_s) + \mathcal{W}_{so}(r, E),$$

with Woods-Saxon form factors

$$f(r, r_i, a_i) = \frac{1}{1 + e^{\frac{r-r_i}{a_i}}}. \quad (21)$$

Two contributions to the surface imaginary potential have been included: one dependent and the other independent of asymmetry, i.e.,

$$W_s(E) = W_s^0(E) + D(N, Z)W_s^1(E). \quad (22)$$

The asymmetry-dependent factor $D(N, Z)$ for protons is just

$$D^p(N, Z) = \frac{N - Z}{A}. \quad (23)$$

In Sec. VII B two different asymmetry dependences $D^n(N, Z)$ for neutrons will be discussed. However, based on the the integrated potential in Sec. IV, we assume the neutron and proton potentials are identical for ^{40}Ca , i.e., $D^p = D^n = 0$. Both surface terms have been parametrized by the same form, which is assumed symmetric about E_F . The latter form is taken from our previous work [18] and consists of the difference of

two functions that cancel at large energies,

$$W_s^i(E) = \omega_4(E, A_s^i, B_{s1}^i, 0) - \omega_2(E, A_s^i, B_{s2}^i, C_s^i), \quad (24)$$

$$\omega_n(E, A_s^i, B_s^i, C_s^i) = A_s^i \Theta(X) \frac{X^n}{X^n + (B_s^i)^n}, \quad (25)$$

where $\Theta(X)$ is Heaviside’s step function and $X = |E - E_F| - C_s^i$. The functions ω_n are very practical for constructing the imaginary potentials, as there are analytical expressions for the corresponding dispersion integrals [64,65]. Figure 4(a) demonstrates the relationship between the shape of $W_s^i(E)$ and its four defining parameters A_s , B_{s1} , B_{s2} , and C_s . It is important to note that the present treatment of the optical potential generates an ℓj -independent representation of the nucleon self-energy, apart from the spin-orbit contribution which is explicitly included. Details of the pole structure of the nucleon self-energy [1] at very low energy that depend on angular momentum and parity are therefore only treated in an average way.

The phase space of particle levels for $E \gg E_F$ is significantly larger than that of hole levels for $E \ll E_F$. Therefore the contributions from two-particle–one-hole states for $E \gg E_F$ will be larger than that for two-hole–one-particle states at $E \ll E_F$. Thus at energies well removed from E_F , the form of the volume imaginary potential should no longer be symmetric about E_F . Hence the following form was assumed:

$$W_v(E) = \omega_4(E, A_v, B_v, 0) + \Delta W_{NM}(E), \quad (26)$$

where $\Delta W_{NM}(E)$ is the energy-asymmetric correction modeled after nuclear-matter calculations. Apart from this correction, the parametrization is just the Jeukenne and Mahaux form [66] used in many DOM analyses.

The energy-asymmetric correction was taken as

$$\Delta W_{NM}(E) = \begin{cases} \alpha \left[\sqrt{E} + \frac{(E_F + E_a)^{3/2}}{2E} - \frac{3}{2} \sqrt{E_F + E_a} \right] & \text{for } E - E_F > E_a, \\ -\omega_2(E, A_v, E_a, 0, E_a) & \text{for } E - E_F < E_a, \\ 0 & \text{otherwise.} \end{cases} \quad (27)$$

This is the same form as assumed in Ref. [6], except for $E - E_F < E_a$, where the form is slightly different but has the advantage of making the calculation of the dispersive correction easier. The parameter α defines the magnitude of the asymmetry correction for $E > E_F$ [see Fig. 4(b)], and Mahaux and Sartor assumed a value of $\alpha = 1.65 \text{ MeV}^{1/2}$. However, the value of this quantity is not constrained theoretically. For example, nuclear-matter calculations with the CDBonn and ArV18 interactions predict very different behavior, see Fig. 2 of Ref. [67]. Fitting these calculated imaginary potentials with Eqs. (26) and (27), we obtained values of $\alpha \approx 0$ and $\alpha = 2.2 \text{ MeV}^{1/2}$ for the two interactions, respectively. In the DOM analysis, the larger values of α do not give good fits,

otherwise the value is not well constrained. Subsequently, we have used a fixed, intermediate value of $\alpha = 0.61 \text{ MeV}^{1/2}$. The uncertainty in α gives rise to uncertainties in the absolute values of the predicted spectroscopic factors and occupation probabilities [6,18].

The dependence of $W_v(E)$ on its defining parameters (A_v , B_v , E_a , and α) is shown in Fig. 4(b). We note that the effect of the energy asymmetry in the volume potential is mainly confined to the deeply bound orbits. In the present description, few data are available to constrain this energy asymmetry. This situation would likely improve if charge densities could be included in the fit procedure.

The Hartree-Fock potential is parametrized in the following way:

$$\mathcal{V}_{\text{HF}}(r, E) = -V_{\text{HF}}^{\text{Vol}}(E) f(r, r_{\text{HF}}, a_{\text{HF}}) + 4V_{\text{HF}}^{\text{Sur}} \frac{d}{dr} f(r, r_{\text{HF}}, a_{\text{HF}}) + V_c(r) + \mathcal{V}_{\text{so}}(r, E),$$

where the Coulomb V_c and real spin-orbit \mathcal{V}_{so} terms have been separated from the volume and surface components. The volume component contains the energy dependence representing nonlocality, which was assumed to be linear below the Fermi energy and by a sum of two exponentials above. The two forms are matched at the Fermi energy as

$$V_{\text{HF}}^{\text{Vol}}(E) = \begin{cases} A_{\text{HF}} \exp\left[-\frac{B_{\text{HF}}}{A_{\text{HF}}}(E - E_F)\right] + C_{\text{HF}} \exp\left[-\frac{D_{\text{HF}}}{C_{\text{HF}}}(E - E_F)\right] & \text{for } E > E_F, \\ A_{\text{HF}} - B_{\text{HF}}(E - E_F) + C_{\text{HF}} - D_{\text{HF}}(E - E_F) & \text{for } E < E_F. \end{cases} \quad (28)$$

As it is important to have the correct Fermi energy in the DOM, the quantity A_{HF} (related to the depth of the Hartree-Fock potential) was not fit, but adjusted to reproduce this quantity. In addition to the standard volume term, a surface term $V_{\text{HF}}^{\text{Sur}}$ is also included. In the fits, $V_{\text{HF}}^{\text{Vol}}$ dominates $V_{\text{HF}}^{\text{Sur}}$ for all but the highest energies. Here the surface and volume components combine to give a “wine-bottle” shape. There is both theoretical and experimental evidence to support such a potential. Relativistic and nonrelativistic nuclear-matter calculations suggest that the magnitude of the real optical-model potential should decrease faster with energy for saturated than for lower density nuclear matter [22,68,69]. When combined with a local-density or more sophisticated approximations, the predicted potentials for finite nuclei have wine-bottle shapes for proton energies around 180–200 MeV [22,70–72]. Satchler has also indicated that a wine-bottle potential allows the description of both elastic and inelastic scattering data at these high energies [73]. The inclusion of a real surface contribution

causes the predicted values of R_{rms}^V to increase at the largest energies as suggested in Fig. 3. It was also found to improve the quality of the fits for these energies.

At high energies, OM potentials generally include an imaginary spin-orbit potential [43]. Given that this term is usually assumed to be zero for lower energies, this implies that the imaginary spin-orbit term is energy dependent. As such, it should give rise to a dispersive correction to the real component. Given these considerations, the total spin-orbit potential was taken as

$$\begin{aligned} \mathcal{U}_{\text{so}}(r, E) &= \mathcal{V}_{\text{so}}(r, E) + i\mathcal{W}_{\text{so}}(r, E) \\ &= \Delta\mathcal{V}_{\text{so}}(r, E) + \left(\frac{\hbar}{m\pi c}\right)^2 [V_{\text{so}} - C_{\text{so}}E \\ &\quad + iW_{\text{so}}(E)] \frac{1}{r} \frac{d}{dr} f(r, r_{\text{so}}, a_{\text{so}}) \frac{\boldsymbol{\ell} \cdot \mathbf{s}}{2}, \end{aligned}$$

where $(\hbar/m\pi c)^2 = 2.0 \text{ fm}^2$ and $\Delta\mathcal{V}_{\text{so}}$ is the dispersive correction determined from the imaginary component \mathcal{W}_{so} . As the imaginary spin-orbit component is generally needed only at high energies, we chose the form

$$W_{\text{so}}(E) = \omega_4(E, A_{\text{so}}, B_{\text{so}}, 0). \quad (29)$$

The dispersive correction $\Delta V_{\text{so}}(E)$ associated with this component from Eq. (4) gives an approximately linear decrease in magnitude of the total real spin-orbit strength over the energy region of interest. Through the term C_{so} , we also include the possibility of an additional linear decrease in the real spin-orbit strength due to nonlocality. However, in the final fit, the C_{so} term is very small (Table VI), suggesting that the dispersive term accounts for most of the energy dependence. Thus, imposition of causality provides a natural way to account for all the linear decrease in the magnitude of the integrated potential J_{so} observed in Fig. 3.

VI. FIT RESULTS

Comparisons of experimental and fitted elastic scattering data are shown in Figs. 5 and 6 for differential cross sections and analyzing powers, respectively. Fitted reaction and total

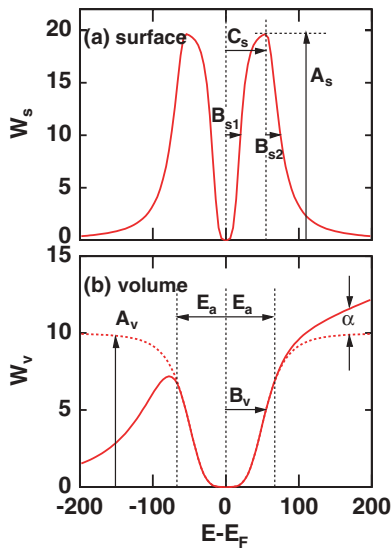


FIG. 4. (Color online) Typical energy dependences of (a) the surface and (b) the volume imaginary potentials. In each case, the meanings of the defining parameters are indicated. For the volume term in (b), the dashed curve indicates the symmetric potential, before the energy asymmetry correction ΔW_{NM} is added.

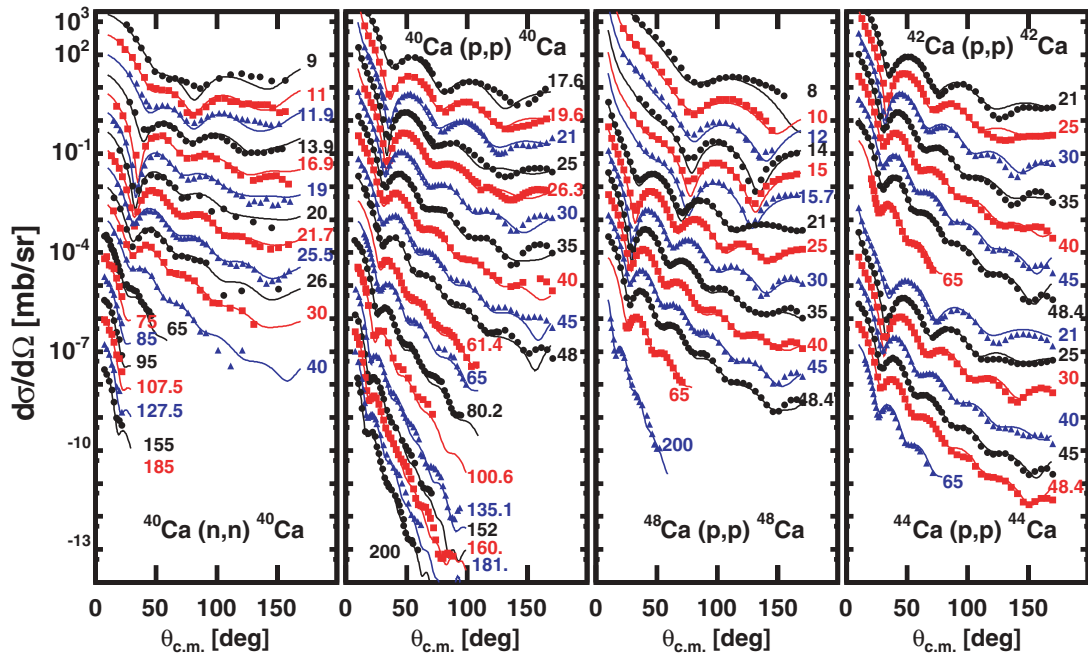


FIG. 5. (Color online) Comparison of experimental (data) and fitted (curves) differential elastic-scattering cross sections. For display purposes, both data and curves for successively larger energies are scaled down by a factor of 4. For $p+^{42}\text{Ca}$, the data and curves are scaled down by an additional factor of 100.

cross sections are displayed in Fig. 7, while the fitted bound-state data from $(e, e'p)$ results are shown in Fig. 8, and the level energies are compared in Fig. 9. The fit parameters are listed in Table VI. For such a large body of data (81 data sets comprising 3569 data points), the excellent agreement

of the fit with just 25 free parameters provides confidence in the predictive power of the DOM calculations. For example, Figs. 10 and 11 compare the DOM predictions to data not included in the fit. The predicted spin-rotation parameters for proton reactions in Fig. 10 describe the experimental data quite

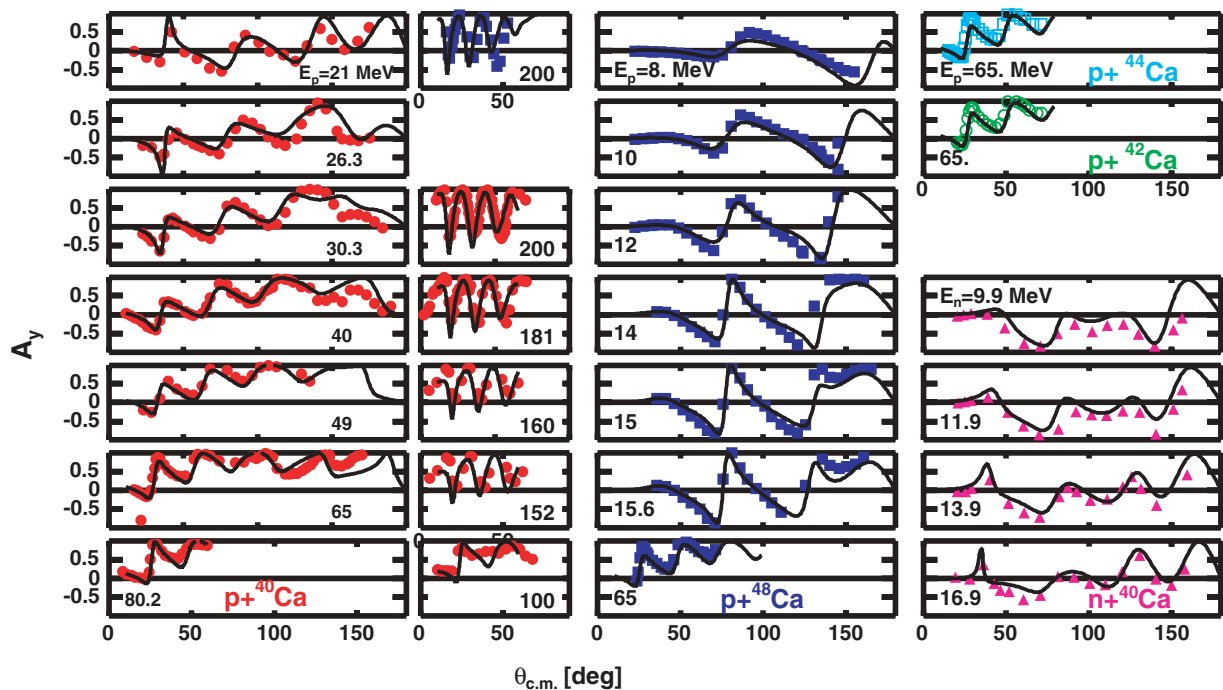


FIG. 6. (Color online) Comparison of experimental and fitted analyzing powers. The data points depicted by the solid circles, solid squares, open circles, open squares, and triangles are for the $p+^{40}\text{Ca}$, $p+^{48}\text{Ca}$, $p+^{42}\text{Ca}$, $p+^{44}\text{Ca}$, and $n+^{40}\text{Ca}$ reactions, respectively.

TABLE VI. Parameters describing the OM potential obtained from fitting of the data.

$B_{\text{HF}} = 0.415$ MeV, $C_{\text{HF}} = 18.29$ MeV,
$D_{\text{HF}} = 0.153$ MeV
$V_{\text{HF}}^{\text{sur}} = 1.81$ MeV, $r_{\text{HF}} = 1.19$ fm, $a_{\text{HF}} = 0.70$ fm
$A_s^0 = 6.19$ MeV, $B_{s1}^0 = 9.82$ MeV, $B_{s2}^0 = 36.94$ MeV
$C_s^0 = 58.1$ MeV
$A_s^1 = 110.34$ MeV, $B_{s1}^1 = 7.82$ MeV, $B_{s2}^1 = 17.70$ MeV
$C_s^1 = 30.0$ MeV
$r_s = 1.27$ fm, $a_s = 0.64$ fm
$A_v = 6.18$ MeV, $B_v = 47.85$ MeV
$r_v = 1.38$ fm, $a_v = 0.63$ fm
$E_a = 60$ MeV (fixed), $\alpha = 0.61$ MeV ^{1/2} (fixed)
$V_{\text{so}} = 5.51$ MeV, $A_{\text{so}} = -4.38$ MeV, $B_{\text{so}} = 208.6$ MeV
$r_{\text{so}} = 1.058$ fm, $a_{\text{so}} = 0.67$ fm, $C_{\text{so}} = -4.5 \times 10^{-4}$
$r_C = 1.31$ fm (fixed)

well. In Fig. 11, the widths of neutron levels in ⁴⁰Ca determined from transfer reactions are also well reproduced. We also note that parameters such as radii and diffuseness properties in Table VI have values that are quite standard.

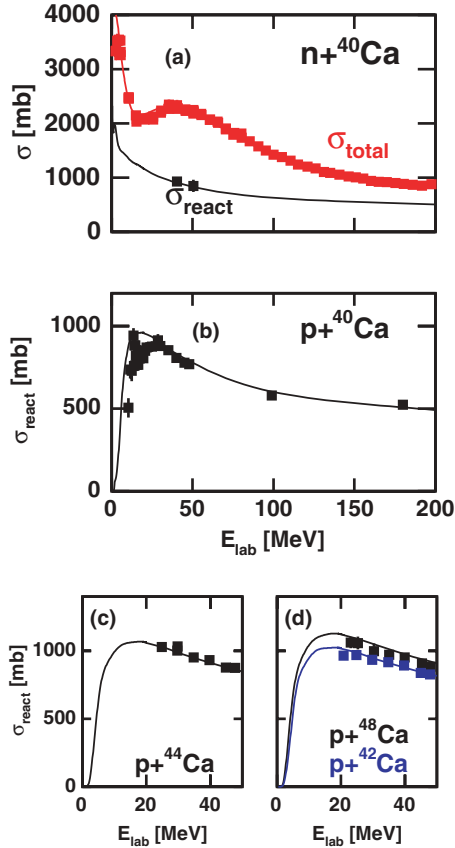


FIG. 7. (Color online) Comparison of experimental and predicted reaction and total scattering cross sections. (a) Total and reaction cross sections for the $n+^{40}\text{Ca}$ reaction. Reaction cross sections for (b) $p+^{40}\text{Ca}$, (c) $p+^{44}\text{Ca}$, and (d) $p+^{42,48}\text{Ca}$ reactions.

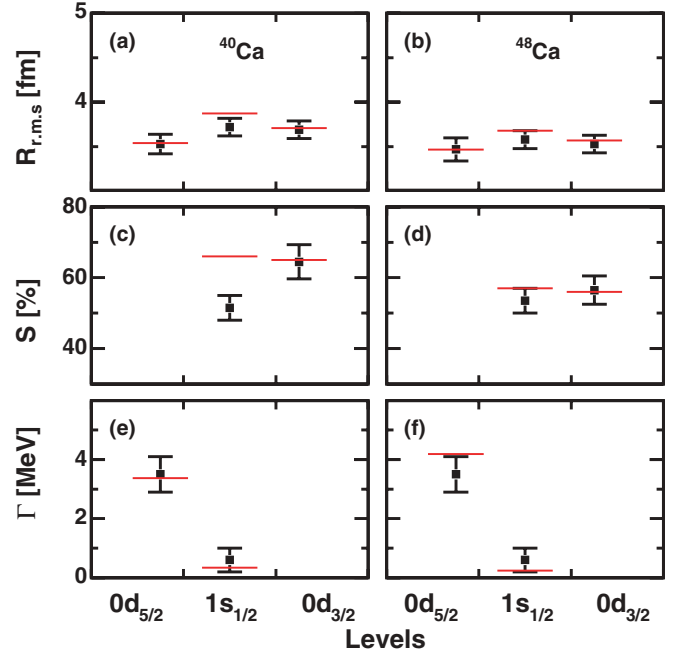


FIG. 8. (Color online) Fitted (horizontal lines) and experimental (data points) level properties for the $0d_{5/2}$, $1s_{1/2}$, and $0d_{3/2}$ proton hole states for ⁴⁰Ca (left panels) and ⁴⁸Ca (right panels). The fitted quantities include the root-mean-squared radius R_{rms} in panels (a) and (b); the spectroscopic factors S expressed as a percentage of the independent-particle-model value in (c) and (d); and the widths Γ of these states in (e) and (f).

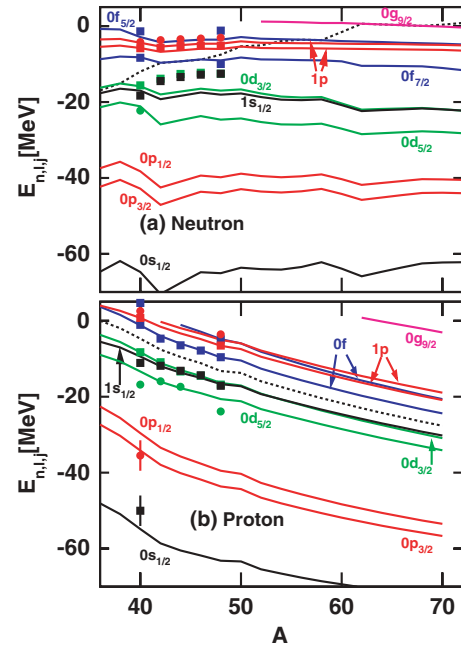


FIG. 9. (Color online) Evolution of single-particle energies with A for Ca isotopes, showing the predictions with the asymmetry-dependence D_2 of Eq. (39) (solid curves), experimental values (Sec. III) (data points), and Fermi energies (dashed curves).

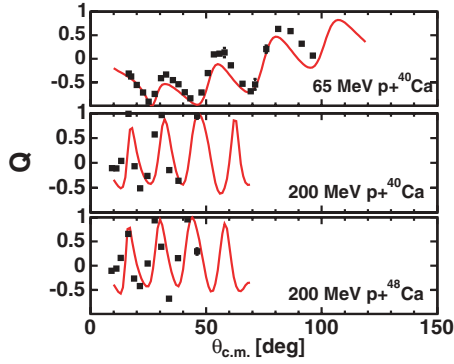


FIG. 10. (Color online) Comparison of experimental and predicted spin-rotation parameters Q .

VII. DISCUSSION

A. Potentials

The energy dependence of the potentials is shown in Fig. 12. The Hartree-Fock potential V_{HF} is dependent on the parameter A_{HF} which is adjusted for each system. The potential plotted in Fig. 12 is for the $p+^{40}\text{Ca}$ system. For the other systems, while the absolute potential will be different, the relative energy dependence is the same.

The two imaginary surface potentials have quite different energy dependences. The asymmetry-dependent or isovector component W_s^1 rises and falls faster with $|E - E_F|$ than the isoscalar component W_s^0 . This is consistent with our previous work, in which the minimum around the Fermi energy for the total imaginary potential was found to be narrower for $p+^{48}\text{Ca}$ compared to $p+^{40}\text{Ca}$ [18]. The elastic-scattering and other positive-energy data constrain the falling part of these potentials, while the rising part is constrained by the $(e, e'p)$ data and the level energies. It is therefore essential to have both positive and negative energy data to fully constrain these potentials.

The fitted potentials are consistent with the integrated potentials and rms radii for the $p+^{40}\text{Ca}$ reaction presented in Fig. 3. The curves in this figure indicate the DOM predictions. The slow falloff with energy of the isoscalar surface potential W_s^0 (seen in Fig. 12) is responsible for the slow falloff of the R_{rms}^W values in Fig. 3(b). The faster falloff for the isovector

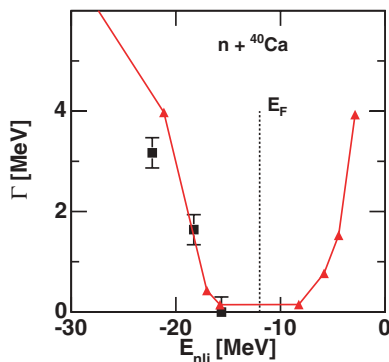


FIG. 11. (Color online) Comparison of experimental and predicted widths of neutron states in ^{40}Ca .

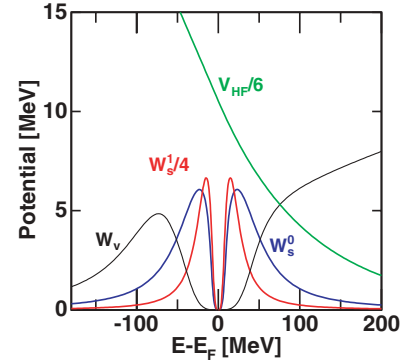


FIG. 12. (Color online) Potentials determined from the fit. The Hartree-Fock potential V_{HF} is for $p+^{40}\text{Ca}$, while the other potentials are system independent.

component is required in order for the J_W values of Figs. 1 and 2 to be largely asymmetry independent by 50 MeV. The surface Hartree-Fock component is responsible for the small increase of R_{rms}^V at the larger energies.

B. Neutron asymmetry dependence

Asymmetry dependences of global optical-model potentials are based on the Lane model [74]. If the nuclear force is charge independent, the optical-model potential for nucleon scattering can be written in the form

$$\mathcal{U} = v_0 + \frac{\mathbf{t} \cdot \mathbf{T}}{A} v_1, \quad (30)$$

where \mathbf{t} and \mathbf{T} represent the nucleon and target isospin operators, and v_0 and v_1 depend in general on position and energy but not on N or Z . For proton and neutron scattering off a target of isospin T_0 with projection T_0 , the mean potential is

$$\begin{aligned} \bar{\mathcal{U}}_n^p &= \left\langle \frac{1}{2} \mp \frac{1}{2} T_0 T_0 \left| \mathcal{U} \right| \frac{1}{2} \mp \frac{1}{2} T_0 T_0 \right\rangle \\ &= v_0 - (\pm) \frac{N-Z}{A} \frac{v_1}{4}. \end{aligned} \quad (31)$$

The real part of the $\pm \frac{N-Z}{A} v_1$ term is associated with the symmetry energy. Global OM parametrizations [16,17] also include a $\pm \frac{N-Z}{A}$ dependence for the surface imaginary potential. Therefore let us consider the consequences of using the standard OM asymmetry dependence in the DOM by setting

$$D_1^n(N, Z) = \pm \frac{N-Z}{A}. \quad (32)$$

For neutrons, this implies that the asymmetry dependence is of the same magnitude but of opposite sign to the fitted proton dependence.

Figure 13 shows experimental total reaction cross sections for $n+^{44}\text{Ca}$. The DOM predictions obtained with Eq. (32) are indicated by the dashed curve and reproduce these experimental results very well.

Neutron spectroscopic factors extracted in a consistent analysis of (p, d) and (d, p) transfer reactions on Ca isotopes [75] are plotted in Fig. 14 as a function of A . Again the

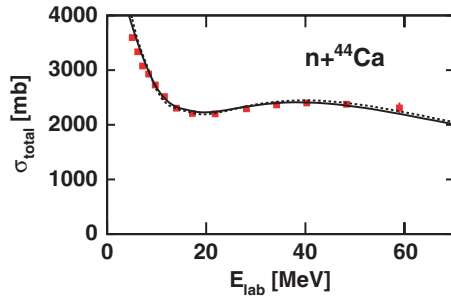


FIG. 13. (Color online) Comparison of DOM predictions to experimental $n+^{44}\text{Ca}$ total cross sections. The dashed and solid curves indicate the predictions using the asymmetry dependences D_1 and D_2 , respectively.

DOM predictions obtained with Eq. (32) are indicated by the dashed curve. One should compare the A dependence of the spectroscopic factors, not the absolute values, as both the data and predictions have absolute uncertainties. Given the fluctuations in the data points, the dashed curve cannot be discounted. However, the experimental data do not show any indication of the rise in the spectroscopic factor with A as suggested by the dashed curve.

In the end, the asymmetry dependence for neutrons implied by Eq. (32) has to be abandoned, as it leads to pathological problems in neutron-rich Ca isotopes. For example, Fig. 15 shows the extrapolated surface potentials $W_s(E)$ for the $p+^{50}\text{Ca}$ and $n+^{50}\text{Ca}$ reactions obtained with Eq. (32). The neutron potential is negative over small energy intervals either side of E_F . As the volume potential is essentially zero for these energies, the total imaginary potential is also negative. In such a case, there is no absorption, but there is unphysical creation of neutrons!

Given the unphysical result for neutrons with the standard OM asymmetry dependence, it is useful to examine how well the asymmetry dependence is determined by OM fits. For this purpose, we searched for other studies that measured elastic scattering for a long chain of isotopes at a fixed energy. We restricted the search to bombarding energies in the $15 < E < 30$ MeV range to avoid compound-elastic

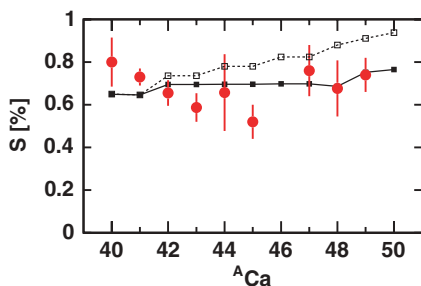


FIG. 14. (Color online) Data points indicate spectroscopic factors deduced by Lee *et al.* [75] for valance neutron hole and particle states in Ca isotopes using (p, d) and (d, p) reactions. The spectroscopic factors are expressed as a percent of the independent-particle-model value. The DOM predictions with the asymmetry dependences D_1 [see Eq. (32)] and D_2 [Eq. (39)] are indicated by the points connected with dashed and solid lines, respectively.

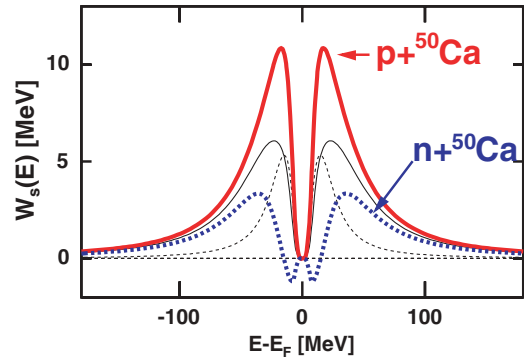


FIG. 15. (Color online) Surface imaginary potentials for $p+^{50}\text{Ca}$ (solid thick curves) and $n+^{50}\text{Ca}$ (dashed thick curves) obtained with the $D_1(N, Z)$ asymmetry dependence. The thin-dashed curves indicate the magnitude of the isovector components while the thin-solid curves are for the isoscalar components.

processes, but where the energies were low enough such that the surface imaginary component was still dominant. In each of the chosen cases, the elastic scattering was measured and fit consistently for each isotope in the chain by the authors of the respective studies. Figure 16 shows systematics of the integrated imaginary potential J_W from these cases, and the lines are fits to the data points. For neutrons [Fig. 16(a)], only one study of $n+^A\text{Mo}$ [76] was found; whereas for protons [Fig. 16(b)], studies of seven reactions from $p+^A\text{Ca}$ to $p+^A\text{Sn}$ [45,77–80] were found. As for the low-energy data in Fig. 1, all the proton reactions show a clear increase in the magnitude of J_W with asymmetry.

Based on the assumed asymmetry dependence of Eq. (32), $|J_W/A|$ would be expected to decrease with asymmetry for neutrons. In fact, as the $p+^A\text{Mo}$ and $n+^A\text{Mo}$ data in Figs. 16(a) and 16(b) are for similar bombarding energies, the slopes of their asymmetry dependences are expected to be approximately equal but opposite in sign. This is not the case, the neutrons in fact show very little asymmetry dependence. It should be noted that the $n+^A\text{Mo}$ data set

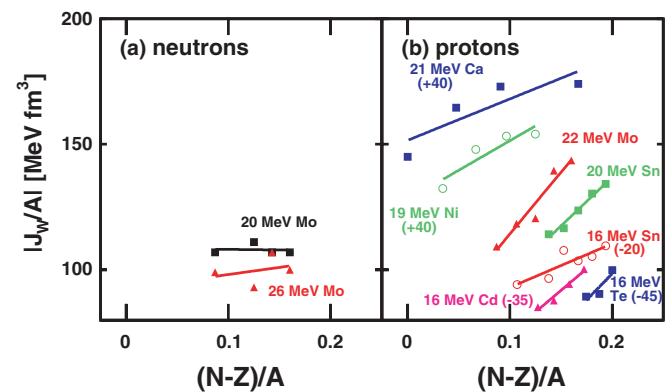


FIG. 16. (Color online) Integrated imaginary potentials for (a) neutrons and (b) protons as a function of asymmetry. The data points are from the elastic-scattering studies of Refs. [45,76–80]. The lines are linear least-square fits to these data. For display purposes, the data and lines are shifted along the y axis by the amounts indicated in parentheses.

was rejected from the CH89 global optical-model fit [17], as these data could not be fit with the assumed parametrization. This fact suggests that either the $n+{}^A\text{Mo}$ data are suspect and not representative or the assumed asymmetry dependence [Eq. (32)] is incorrect. Therefore unlike for protons, the sign and magnitude of the asymmetry dependence for neutrons has not been established in prior studies, and thus there is a need for future measurements to address this.

Satchler [81] gives a microscopic justification of the standard asymmetry dependence [Eq. (32)] based on the average interaction of a projectile nucleon with the individual target nucleons. Taking into account the difference between the mean in-medium neutron-proton $\langle\sigma_{np}\rangle$ and proton-proton $\langle\sigma_{pp}\rangle$ scattering cross sections, the imaginary potential is

$$W^p = \frac{\hbar v \rho_N}{2} \left(\frac{N}{A} \langle\sigma_{np}\rangle + \frac{Z}{A} \langle\sigma_{pp}\rangle \right) \quad (33)$$

$$= \frac{\hbar v \rho_N}{4} (\langle\sigma_{np}\rangle + \langle\sigma_{pp}\rangle) + \frac{N-Z}{A} \frac{\hbar v \rho_N}{4} (\langle\sigma_{np}\rangle - \langle\sigma_{pp}\rangle) \quad (34)$$

$$= W_0 + \frac{N-Z}{A} W_1, \quad (35)$$

where v is the incident nucleon's velocity inside the target nucleus which has a nucleon density of ρ_N . Similarly, for an incident neutron,

$$W^n = \frac{\hbar v \rho_N}{2} \left(\frac{N}{A} \langle\sigma_{nn}\rangle + \frac{Z}{A} \langle\sigma_{np}\rangle \right) \quad (36)$$

$$= \frac{\hbar v \rho_N}{4} (\langle\sigma_{np}\rangle + \langle\sigma_{nn}\rangle) - \frac{N-Z}{A} \frac{\hbar v \rho_N}{4} (\langle\sigma_{np}\rangle - \langle\sigma_{nn}\rangle), \quad (37)$$

as $\langle\sigma_{nn}\rangle \simeq \langle\sigma_{pp}\rangle$, then

$$W^n = W_0 \pm \frac{N-Z}{A} W_1. \quad (38)$$

The correlations implicit in this derivation are short range and thus are applicable to the volume imaginary potential. Therefore, this potential should have an isovector term of strength $\pm \frac{N-Z}{A}$. In the present work, we have assumed that this term is small relative to the asymmetry dependence of the surface potential, but for infinite nuclear matter this term will give the total asymmetry dependence of the imaginary potential. It will be responsible for the asymmetry dependence of the occupation probabilities in infinite nuclear matter such as those predicted in Ref. [3].

For surface absorption, the situation is more complex. The total absorption is a result of couplings of the incident nucleon to many collective modes. Thus the overall asymmetry dependence may have contributions from many of these modes. Let us consider just a few of the possible long-range correlations, i.e., collective vibrations and Gamow-Teller resonances. These correlations are illustrated in Fig. 17. The couplings of particles and holes to collective 2^+ vibrational modes are considered in Figs. 17(a) and 17(b), respectively. From parity considerations, the collective 2^+ mode must be comprised of particle-hole excitations, where the particles and holes have the same parity.

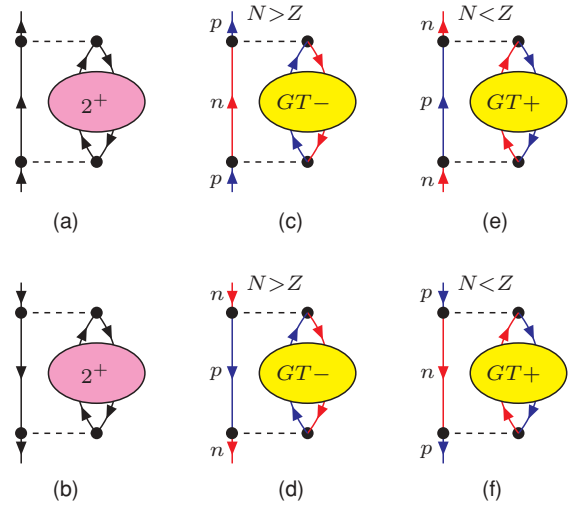


FIG. 17. (Color online) Feynman diagrams of important long-range correlations considered in this work. These include couplings of (a) particles and (b) holes to collective 2^+ vibrations. Couplings to giant Gamow-Teller resonances are diagramed in (c) and (d) for nuclei with $N > Z$ and in (e) and (f) for $N < Z$. The Gamow-Teller resonances are labeled by the sign of the change in isospin projection $\Delta M_T = \pm 1$.

For ${}^{40}\text{Ca}$, particles will be in the negative parity fp shell, while holes are in the positive parity sd shell. These vibrational excitations will therefore be suppressed in ${}^{40}\text{Ca}$. In going to ${}^{48}\text{Ca}$ by adding neutrons to the $0f_{7/2}$ level, the collective 2^+ strength should be stronger as neutron particles and holes are both in the fp shell. As protons and neutrons (particles and holes) can couple to these collective 2^+ excitations, then for both particle types, the contribution to the surface imaginary potential from these couplings will increase in going from ${}^{40}\text{Ca}$ to ${}^{48}\text{Ca}$.

The sum-rule strength of the giant Gamow-Teller resonance has a strong asymmetry dependence and thus coupling to this resonance may be important. For $N > Z$, only proton particles [Fig. 17(c)] and neutron holes [Fig. 17(d)] couple to the Gamow-Teller with the change in isospin projection of $\Delta M_T = -1$, while for $N < Z$, only neutron particles [Fig. 17(e)] and proton holes [Fig. 17(f)] couple to the Gamow-Teller with $\Delta M_T = +1$. These possible couplings are governed by isospin selection rules. Parity conservation is also important in these coupling schemes. For example, in Fig. 17(d), the typical neutron hole in ${}^{48}\text{Ca}$ has negative parity ($0f_{7/2}$ level). In the charge-changing interaction, this neutron couples to a proton hole and the 1^+ Gamow-Teller resonances. As the latter have positive parity, the proton hole must have negative parity. However, typical proton holes in ${}^{48}\text{Ca}$ (sd shell) have positive parity, so these interactions will be suppressed.

For proton elastic scattering, we would expect an increase in absorption in going from ${}^{40}\text{Ca}$ to ${}^{48}\text{Ca}$ because of the coupling to the Gamow-Teller collective mode. On the other hand, we expect no change for neutrons, as they do not couple to this resonance. Also, as particles and holes do not couple to this resonance in the same manner, the surface imaginary

potential may not be symmetric about the Fermi energy as assumed in Eq. (24). We also note that interference between different modes may occur that can be described in the Faddeev formalism developed in Ref. [82] and applied in Ref. [83].

The examples of coupling to vibrational and Gamow-Teller collective modes clearly indicate that an asymmetry dependence different from the $\pm \frac{N-Z}{A}$ dependence assumed in global OM might be expected from long-range correlations. However, given that the surface potential contains absorption from coupling to many different collective modes, one cannot at present predict the relationship between the dependences for neutron and protons. We have also shown experimentally that the asymmetry dependence for neutron particles in elastic scattering is not determined. Given these uncertainties, we have chosen to investigate the consequences of setting the asymmetry dependence for neutrons to zero. Thus we consider a second asymmetry dependence

$$D_2^p(N, Z) = \frac{N-Z}{A}, \quad D_2^n = 0. \quad (39)$$

Such a dependence is suggested by the flat behavior of J_W/A for the $n+^{A}\text{Mo}$ data in Fig. 16(a). The predicted total reaction cross sections for $n+^{44}\text{Ca}$ are now indicated by the solid curve in Fig. 13. Both this curve and the dashed curves obtained with the first parametrization [Eq. (32)] are almost identical and in good agreement with the data. Therefore this quantity is not very sensitive to the asymmetry dependence.

The mass dependence of neutron spectroscopic factors is shown in Fig. 14. The new predictions (solid curve) have a rather flat mass dependence significantly different from the previous predictions (dashed curve) obtained with D_1^n [Eq. (32)]. The new predicted dependence is not unexpected, because the imaginary potential is now independent of asymmetry, and thus the spectroscopic factors should have little A dependence. In fact, this dependence seems to be more consistent with the experimental data than that based on D_1^n . Finally as $D_2^n = 0$, there is no possibility of having an unphysical imaginary potential which changes sign.

Energies of bound neutron levels for $^{42-48}\text{Ca}$ are also compared to DOM predictions in Fig. 9. While the energies of the $0f$ and $1p$ levels are reasonably well described, there is an apparent discrepancy for the $0d_{3/2}$ and $1s_{1/2}$ levels, which are almost degenerate. This discrepancy worsens for the heavier Ca isotopes where these levels approach the $0f_{7/2}$ level. A similar discrepancy also exists when compared with the prediction of the first asymmetry dependence D_1 . It is difficult to understand these experimental results. In the DOM, one would require a large dispersive correction to push these levels toward the $0f_{7/2}$ state, and this would have serious consequences for levels on the other side of the Fermi energy, which are not observed.

It may be that the full strengths of the $0d_{3/2}$ and $1s_{1/2}$ levels have not been observed experimentally and that there is missing strength at lower energies that would pull down the average energies of these levels in line with the predictions. For ^{48}Ca , the worst case, the observed strengths of the $0d_{3/2}$ and $1s_{1/2}$ levels are confined to a single fragment, and any missing strength must be in the continuum. In (p, d) reactions, the observed fragments are reported to have a spectroscopic

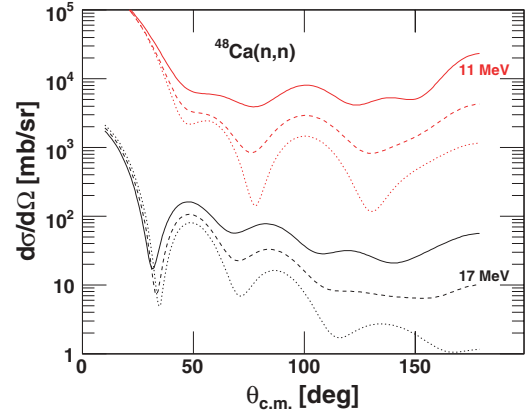


FIG. 18. (Color online) Predicted $n+^{48}\text{Ca}$ elastic-scattering differential cross sections at 11 and 17 MeV. The solid and dashed curves were obtained with the D_1 and D_2 asymmetry dependences, while the dotted curves assume the same imaginary potential as fitted for protons.

strength close to the IPM limit [84,85]. If this is correct, then there is no significant missing strength indicating that there is some important physics missing from our DOM analysis. On the other hand, for (d, t) reactions, the reported strength of these fragments is significantly less [86]. For example, the $0d_{3/2}$ fragment carries only 30% of the single-particle strength in the (d, t) reaction, while Ref. [85] reports 90%. This suggests that it is useful to initiate a search for missing strength to clarify the situation.

Finally, let us consider the sensitivity of the elastic-scattering differential cross section to the form of $D(N, Z)$. Figure 18 shows predicted $n+^{48}\text{Ca}$ differential cross sections at energies of 11 and 17 MeV. The solid and dashed curves show the predictions with D_1 and D_2 . For the dotted curves, we used the same imaginary potential as fitted for protons. The large dependence of the magnitude of these differential cross sections on the asymmetry dependence of the imaginary potential suggests that measurements of these quantities could significantly improve our knowledge of neutron correlations.

C. Extrapolating to the drip lines

To extrapolate beyond the region of known masses, one must estimate the Fermi energies for these nuclei. The Fermi

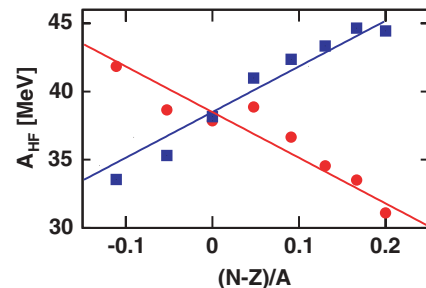


FIG. 19. (Color online) Asymmetry dependence of the parameter A_{HF} for both protons (squares) and neutrons (circles). The data points were obtained in the DOM calculations by reproducing the experimental Fermi energies. The lines are fits to these results.

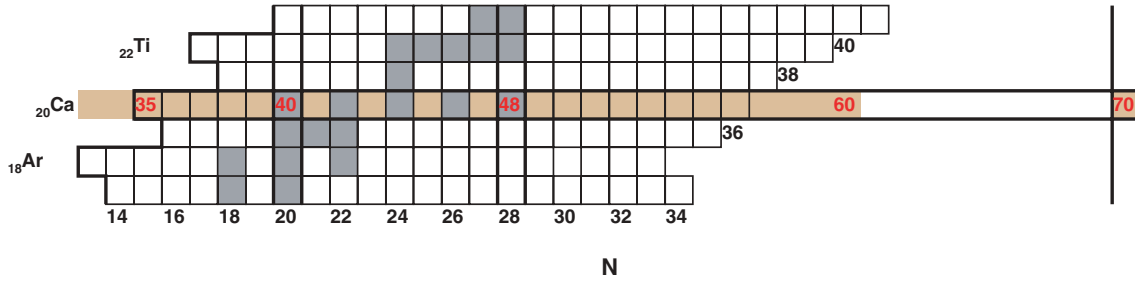


FIG. 20. (Color online) Chart of nuclides in the region of Ca showing the known isotopes. The shaded region for Ca indicates the predicted isotopes that are particle bound using the D_2 asymmetry dependence. The darker boxes correspond to stable nuclei.

energy is related to the parameter A_{HF} . The value of this quantity determined from DOM calculations with $D_2(N, Z)$ is plotted as a function of asymmetry in Fig. 19 for the region of known Ca masses. They follow the expected behavior consistent with the Lane potential in Eq. (31). The lines in Fig. 19 are fits to these results with

$$A_{HF}^p = 38.5 \pm 33.5 \frac{N - Z}{A} \text{ MeV.}$$

With these values of A_{HF} , the Fermi energy in the region of unknown masses is determined by an iterative procedure. Starting with an initial value of E_F , DOM predictions for the valence levels are made from which a new value of E_F is determined. The proton and neutron energy levels determined by this procedure are displayed in Fig. 9.

From these levels, we determined the proton and neutron drip lines. Figure 20 shows the chart of nuclides in the Ca region, where the predicted bound Ca isotopes are shaded. The last proton-bound nucleus is predicted to be ^{33}Ca for which the $0d_{3/2}$ proton is bound by 0.4 MeV. Experimentally, the ^{34}Ca nucleus is thought to be proton unbound, while ^{35}Ca is proton bound [87]. On the neutron-rich side, the predictions indicate that there may not be a well-defined separation between neutron-bound and unbound nuclei. We predict that ^{60}Ca and ^{70}Ca are neutron bound, but the intermediate nuclides are unbound. ^{60}Ca is predicted to be bound by 4.5 MeV and ^{70}Ca by only 170 keV. If neighboring nuclei in the $N = 50$ shell are also bound, one can envisage a reef of particle-stable nuclei offshore from the mainland of other particle-bound systems. While these predictions have considerable uncertainty because of the degree of extrapolation and the need for confirmation of the assumed neutron asymmetry dependence, they suggest the possibility of a more complicated neutron-drip region

than commonly anticipated. In the future, when data at larger asymmetries for protons and neutrons can be included in the DOM analysis, it should be possible to generate a more reliable extrapolation to the drip lines.

D. Occupation probabilities

With the fitted potentials, occupation probabilities calculated for protons in ^{40}Ca and ^{48}Ca are displayed in Fig. 21. Results extrapolated for ^{60}Ca are also shown. There is some uncertainty associated with the absolute values of these probabilities. For instance, the parameter α , defining the energy asymmetry of the volume imaginary potential (see Sec. V), is not constrained in the fits, and variation of this parameter leads to scaling of the occupation probabilities [6,18]. One should therefore concentrate on the relative difference in the probabilities between the three isotopes. The protons show a significant difference: compared to ^{40}Ca , the occupation probabilities for ^{48}Ca and ^{60}Ca are further reduced from unity below the Fermi surface and further enhanced from zero above. The predicted effect is larger for ^{60}Ca . This implies that protons feel stronger correlations in the more neutron-rich nucleus. The differences in occupation are mainly confined to levels near the Fermi surface. The $0s$ and $0p$ levels show very little asymmetry dependence. Their occupation probabilities are dominated by the effects of short-range correlations. Their asymmetry dependence is therefore more strongly connected to any asymmetry dependence of the volume imaginary component, which is absent in the present calculations.

The predictions for neutrons obtained with Eq. (39) are shown in Fig. 22. They show little asymmetry dependence, which is not surprising as the strength of surface imaginary

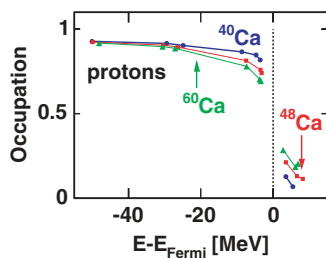


FIG. 21. (Color online) Occupation probabilities predicted for protons in ^{40}Ca (circles), ^{48}Ca (squares), and ^{60}Ca (triangles).

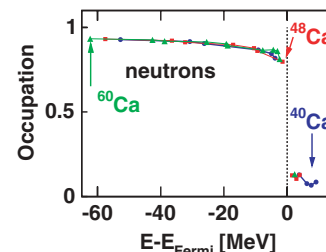


FIG. 22. (Color online) Same as Fig. 21, but for neutrons.

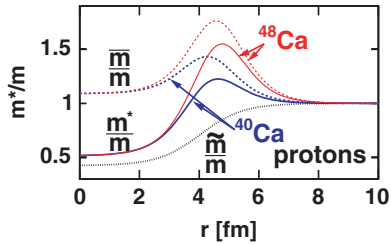


FIG. 23. (Color online) Predicted effective masses relative to the nucleon mass for protons. The momentum-dependent effective masses \tilde{m}/m in ^{40}Ca are given by the dotted curve; results for ^{48}Ca are similar. The energy-dependent effective masses are indicated by the dashed curves, while the solid curves represent the total effective masses. Thick and thin curves identify ^{40}Ca and ^{48}Ca , respectively.

potential is assumed to be identical for all three Ca isotopes, i.e., $D_2 = 0$.

E. Effective masses

Proton effective masses at the corresponding Fermi energy E_F obtained from the DOM calculations are plotted in Fig. 23. The momentum-dependent effective masses \tilde{m}/m are shown only for ^{40}Ca . The results for ^{48}Ca are similar with a slightly larger radius. As for the occupation probabilities, the proton's energy-dependent \bar{m}/m and total m^*/m effective masses show significant difference between ^{40}Ca and ^{48}Ca . The larger surface imaginary component for ^{48}Ca gives rise to an increased enhancement of the proton effective mass in the surface.

F. Neutron knock-out reactions

Our study of correlations has only addressed nuclei with $N \geq Z$. In the case of $N < Z$, the role of the protons and neutrons should be reversed, and thus instead of Eq. (39), we might consider a different asymmetry dependence in this region, i.e.,

$$D_3^p(N, Z) = 0, \quad D_3^n(N, Z) = -\frac{N - Z}{A}. \quad (40)$$

Qualitatively such a dependence for neutrons is supported by the small spectroscopic factors measured in neutron knock-out reactions from proton-rich nuclei and thus require a large imaginary potential. Gade *et al.* found the spectroscopic factor for the $0d_{3/2}$ neutrons in ^{32}Ar was only 24% of that predicted by many-body shell-model theory [4] and thus even a smaller percentage of the IPM value. This is an exceedingly small spectroscopic factor for a valence level. Compare this to the spectroscopic factors of $0d_{3/2}$ protons which change from $65.5\% \pm 4.8\%$ to $56.5\% \pm 4.0\%$ of the IPM value in going from

^{40}Ca to ^{48}Ca [38,39]. To achieve such a small value for neutrons in ^{32}Ar with the DOM (using the D_3 asymmetry dependence), the magnitude of W_s^1 must be significantly larger than we determined for protons. These results indicate the need for measurements of elastic scattering and other data for $N < Z$ to allow the extension of the present DOM analysis to this region to provide a more global view of correlations.

VIII. CONCLUSIONS

A dispersive-optical-model analysis of elastic-scattering angular distributions, analyzing powers, reaction and total cross sections, single-particle level energies, widths, rms radii, and spectroscopic factors was undertaken to deduce the optical-model potential at both positive and negative energies. The asymmetry dependence of the surface imaginary potential for protons was constrained for Ca isotopes by fitting $p+^{40,42,44,48}\text{Ca}$ and $n+^{40}\text{Ca}$ data. However, for neutrons, there are not enough existing data to constrain the asymmetry dependence. Therefore two asymmetry dependencies for neutrons were considered. The first, based on global optical-model fits where the asymmetry dependence for neutrons is of the same magnitude but opposite sign, was found to give unphysical results for heavy Ca isotopes. We also considered the consequences of neutrons having no asymmetry dependence. This was found to better describe systematics of spectroscopic factors in (d, p) or (p, d) reactions.

From the fitted potentials, the occupation probabilities and effective masses were derived. These indicate that for $N > Z$, protons experience stronger correlations for heavier Ca isotopes. This is reflected in reduced (enhanced) occupation probabilities just below (above) the Fermi surface and the enhanced effective mass in the nuclear surface.

The dispersive optical provides a natural framework for data-driven extrapolations to the drip lines. In the present work, single-particle levels were extrapolated to heavier and lighter Ca isotopes and the proton and neutron drip lines were calculated. The predicted proton drip line is at ^{33}Ca whereas the experimental location is at ^{35}Ca . On the neutron-rich side, it is predicted that ^{60}Ca and ^{70}Ca are bound, but the intermediate nuclides are not. With future proton and neutron data at more extreme asymmetries, a more reliable extrapolation can be expected.

ACKNOWLEDGMENTS

This work was supported by the U.S. Department of Energy, Division of Nuclear Physics under Grant DE-FG02-87ER-40316 and the U.S. National Science Foundation under Grant PHY-0652900.

- [1] W. H. Dickhoff and C. Barbieri, Prog. Part. Nucl. Phys. **52**, 377 (2004).
 [2] D. Rohe, C. S. Armstrong, R. Asaturyan, O. K. Baker, S. Bueltmann, C. Carasco, D. Day, R. Ent, H. C. Fenker, K. Garrow *et al.*, Phys. Rev. Lett. **93**, 182501 (2004).

- [3] T. Frick, H. Mütter, A. Rios, A. Polls, and A. Ramos, Phys. Rev. C **71**, 014313 (2005).
 [4] A. Gade, D. Basin, B. A. Brown, C. M. Campbell, J. A. Church, D. C. Dinca, J. Enders, T. Glasmacher, P. G. Hansen, Z. Hu *et al.*, Phys. Rev. Lett. **93**, 042501 (2004).

- [5] W. H. Dickhoff and D. Van Neck, *Many-Body Theory Exposed!* (World Scientific, New Jersey, 2005).
- [6] C. Mahaux and R. Sartor, *Adv. Nucl. Phys.* **20**, 1 (1991).
- [7] C. Mahaux and R. Sartor, *Phys. Rev. C* **36**, 1777 (1987).
- [8] J.-P. Jeukenne, C. H. Johnson, and C. Mahaux, *Phys. Rev. C* **38**, 2573 (1988).
- [9] C. Mahaux and R. Sartor, *Nucl. Phys.* **A484**, 205 (1988).
- [10] C. Mahaux and R. Sartor, *Nucl. Phys.* **A503**, 525 (1989).
- [11] W. Tornow, Z. P. Chen, and J. P. Delaroche, *Phys. Rev. C* **42**, 693 (1990).
- [12] Y. Wang, C. C. Foster, R. D. Polak, J. Rapaport, and E. J. Stephenson, *Phys. Rev. C* **47**, 2677 (1993).
- [13] A. Molina, R. Capote, J. M. Quesada, and M. Lozano, *Phys. Rev. C* **65**, 034616 (2002).
- [14] M. M. Nagadi, C. R. Howell, W. Tornow, G. J. Weisel, M. A. Al-Ohali, R. T. Braun, H. R. Setze, Z. Chen, R. L. Walter, J. P. Delaroche *et al.*, *Phys. Rev. C* **68**, 044610 (2003).
- [15] Z. Chen, R. L. Walter, W. Tornow, G. J. Weisel, and C. R. Howell, *J. Phys. G: Nucl. Part. Phys.* **30**, 1847 (2004).
- [16] F. D. B. Jr. and G. W. Greenlees, *Phys. Rev.* **182**, 1190 (1969).
- [17] R. L. Varner, W. J. Thompson, T. L. McAbee, E. J. Ludwig, and T. B. Clegg, *Phys. Rep.* **201**, 57 (1991).
- [18] R. J. Charity, L. G. Sobotka, and W. H. Dickhoff, *Phys. Rev. Lett.* **97**, 162503 (2006).
- [19] F. Perey and B. Buck, *Nucl. Phys.* **32**, 353 (1962).
- [20] A. Nadasen, P. Schwandt, P. P. Singh, W. W. Jacobs, A. D. Bacher, P. T. Debevec, M. D. Kaitchuck, and J. T. Meek, *Phys. Rev. C* **23**, 1023 (1981).
- [21] R. J. Glauber and P. Osland, *Phys. Lett.* **B80**, 401 (1979).
- [22] D. P. Murdock and C. J. Horowitz, *Phys. Rev. C* **35**, 1442 (1987).
- [23] H. Sakaguchi, M. Yosoi, M. Nakamura, T. Noro, H. Sakamoto, T. Ichihara, M. Ieiri, Y. Takeuchi, H. Togura, T. Tsutsumi *et al.*, *J. Phys. Soc. Jpn. Suppl.* **55**, 61 (1986).
- [24] W. Bauhoff, *At. Data Nucl. Data Tables* **35**, 429 (1986).
- [25] C. I. Zanelli, P. P. Urone, J. L. Romero, F. P. Brady, M. L. Johnson, G. A. Needham, J. L. Ullmann, and D. L. Johnson, *Phys. Rev. C* **23**, 1015 (1981).
- [26] D. G. Foster Jr. and D. W. Glasgow, *Phys. Rev. C* **3**, 576 (1971).
- [27] D. C. Larson, J. Harvey, and N. M. Hill, *Tech. Rep. BNL-BNS-51245*, 1980 (unpublished).
- [28] C. I. Zanelli, F. P. Brady, J. L. Romero, C. M. Castaneda, and D. L. Johnson, *Phys. Rev. C* **33**, 66 (1986).
- [29] W. P. Abfalterer, F. B. Bateman, F. S. Dietrich, R. W. Finlay, R. C. Haight, and G. L. Morgan, *Phys. Rev. C* **63**, 044608 (2001).
- [30] H. S. Camarda, T. W. Phillips, and R. M. White, *Phys. Rev. C* **34**, 810 (1986).
- [31] J. R. Erskine, A. Marinov, and J. P. Schiffer, *Phys. Rev.* **142**, 633 (1966).
- [32] A. N. James, P. T. Andrews, P. Kirkby, and B. G. Lowe, *Nucl. Phys.* **A138**, 145 (1969).
- [33] D. H. Youngblood, R. L. Kozub, R. A. Kenefick, and J. C. Hiebert, *Phys. Rev. C* **2**, 477 (1970).
- [34] D. J. Millener and P. E. Hodgson, *Nucl. Phys.* **A209**, 59 (1973).
- [35] P. Doll, G. J. Wagner, K. T. Knöpfle, and G. Mairle, *Nucl. Phys.* **A263**, 210 (1976).
- [36] M. Matoba, O. Iwamoto, Y. Uozumi, T. Sakae, N. Koori, T. Fujiki, H. Ohgaki, H. Ijiri, T. Maki, and M. Nakano, *Phys. Rev. C* **48**, 95 (1993).
- [37] Y. Uozumi, N. Kikuzawa, T. Sakae, M. Matoba, K. Kinoshita, T. Sajima, H. Ijiri, N. Koori, M. Nakano, and T. Maki, *Phys. Rev. C* **50**, 263 (1994).
- [38] G. J. Kramer, H. P. Blok, J. F. J. van den Brand, H. J. Bulten, R. Ent, E. Jans, J. B. J. M. Lanen, L. Lapikás, H. Nann, E. N. M. Quint *et al.*, *Phys. Lett.* **B227**, 199 (1989).
- [39] G. J. Kramer, H. P. Blok, and L. Lapikás, *Nucl. Phys.* **A679**, 267 (2001).
- [40] L. Lapikás (private communication).
- [41] J.-P. Jeukenne, C. Mahaux, and R. Sartor, *Phys. Rev. C* **43**, 2211 (1991).
- [42] J. F. Dicello, G. Igo, W. T. Leland, and F. G. Perey, *Phys. Rev. C* **4**, 1130 (1971).
- [43] W. T. H. van Oers, *Phys. Rev. C* **3**, 1550 (1971).
- [44] E. T. Boschitz, R. W. Bercaw, and J. S. Vincent, *Phys. Lett.* **13**, 322 (1964).
- [45] R. H. McCamis, T. N. Nasr, J. Birchall, N. E. Davison, W. T. H. van Oers, P. J. T. Verheijen, R. F. Carlson, A. J. Cox, B. C. Clark, E. D. Cooper *et al.*, *Phys. Rev. C* **33**, 1624 (1986).
- [46] D. L. Watson, J. Lowe, J. C. Dore, R. M. Craig, and D. J. Baugh, *Nucl. Phys.* **A92**, 193 (1967).
- [47] V. Hnizdo, O. Karban, J. Lowe, G. W. Greenlees, and W. Makofske, *Phys. Rev. C* **3**, 1560 (1971).
- [48] L. N. Blumberg, E. E. G. Gross, A. van der Woude, A. Zucker, and R. H. Bassel, *Phys. Rev.* **147**, 812 (1966).
- [49] R. M. Craig, J. C. Dore, J. Lowe, and D. L. Watson, *Nucl. Phys.* **86**, 113 (1966).
- [50] C. B. Fulmer, J. B. Ball, A. Scott, and M. L. Whiten, *Phys. Rev.* **181**, 1565 (1969).
- [51] T. Noro, H. Sakaguchi, M. Nakamura, K. Hatanaka, F. Ohtani, H. Sakamoto, and S. Kobayashi, *Nucl. Phys.* **A366**, 189 (1981).
- [52] P. Schwandt, H. O. Meyer, W. W. Jacobs, A. D. Bacher, S. E. Vigdor, M. D. Kaitchuck, and T. R. Donoghue, *Phys. Rev. C* **26**, 55 (1982).
- [53] H. Seifert, Ph.D. thesis, University of Maryland, 1990.
- [54] C. Rolland, B. Geoffrion, N. Marty, M. Morlet, B. Tatischeff, and A. Willis, *Nucl. Phys.* **80**, 625 (1966).
- [55] H. S. Liers, *Nucl. Phys.* **A170**, 616 (1971).
- [56] J. C. Lombardi, R. N. Boyd, R. Arking, and A. B. Robbins, *Nucl. Phys.* **A188**, 103 (1972).
- [57] W. Tornow, E. Woye, G. Mack, C. E. Floyd, K. Murphy, P. P. Guss, S. A. Wender, R. C. Byrd, R. L. Walter, T. B. Clegg *et al.*, *Nucl. Phys.* **A385**, 373 (1982).
- [58] J. Rapaport, J. D. Carlson, D. Bainum, T. S. Cheema, and R. W. Finlay, *Nucl. Phys.* **A286**, 232 (1977).
- [59] G. M. Honoré, W. Tornow, C. R. Howell, R. S. Pedroni, R. C. Byrd, R. L. Walter, and J. P. Delaroche, *Phys. Rev. C* **33**, 1129 (1986).
- [60] R. Alarcon, J. Rapaport, and R. W. Finlay, *Nucl. Phys.* **A462**, 413 (1987).
- [61] R. P. De Vito, S. M. Austin, W. Sterrenburg, and U. E. P. Berg, *Phys. Rev. Lett.* **47**, 628 (1981).
- [62] J. H. Osborne, F. P. Brady, J. L. Romero, J. L. Ullmann, D. S. Sorenson, A. Ling, N. S. P. King, R. C. Haight, J. Rapaport, R. W. Finlay *et al.*, *Phys. Rev. C* **70**, 054613 (2004).
- [63] G. W. Greenlees, G. J. Pyle, and Y. C. Tang, *Phys. Rev.* **171**, 1115 (1968).
- [64] J. M. VanderKam, G. J. Weisel, and W. Tornow, *J. Phys. G: Nucl. Part. Phys.* **26**, 1787 (2000).
- [65] J. M. Quesada, R. Capote, A. Molina, M. Lozano, and J. Raynal, *Phys. Rev. C* **67**, 067601 (2003).
- [66] J. P. Jeukenne and C. Mahaux, *Nucl. Phys.* **A394**, 445 (1983).
- [67] H. Muther and W. H. Dickhoff, *Phys. Rev. C* **72**, 054313 (2005).
- [68] H.-P. Duerr, *Phys. Rev.* **109**, 1347 (1958).

- [69] J.-P. Jeukenne, A. Lejeune, and C. Mahaux, *Phys. Rev. C* **16**, 80 (1977).
- [70] L. G. Arnold, B. C. Clark, R. L. Mercer, and P. Schwandt, *Phys. Rev. C* **23**, 1949 (1981).
- [71] H. O. Meyer, P. Schwandt, G. L. Moake, and P. P. Singh, *Phys. Rev. C* **23**, 616 (1981).
- [72] E. Bauge, J. P. Delaroche, and M. Girod, *Phys. Rev. C* **58**, 1118 (1998).
- [73] G. R. Satchler, *Nucl. Phys.* **A394**, 349 (1983).
- [74] A. M. Lane, *Nucl. Phys.* **35**, 676 (1962).
- [75] J. Lee, J. A. Tostevin, B. A. Brown, F. Delaunay, W. G. Lynch, M. J. Saelim, and M. B. Tsang, *Phys. Rev. C* **73**, 044608 (2006).
- [76] J. Rapaport, T. S. Cheema, D. E. Bainum, R. W. Finlay, and J. D. Carlson, *Nucl. Phys.* **A313**, 1 (1979).
- [77] P. Kossanyi-Demay, R. de Swiniarski, and C. Glashauser, *Nucl. Phys.* **A94**, 513 (1967).
- [78] W. Makofske, W. Savin, H. Ogata, and T. H. Kruse, *Phys. Rev.* **174**, 1429 (1968).
- [79] E. Cereda, M. Pignanelli, S. Micheletti, H. V. vonGeramb, M. N. Harakeh, R. De Leo, G. D'Erasmus, and A. Pantaleo, *Phys. Rev. C* **26**, 1941 (1982).
- [80] S. D. Wassenaar, P. J. van Hall, S. S. Klein, G. J. Nijgh, J. H. Polane, and O. J. Poppema, *J. Phys. G: Nucl. Part. Phys.* **15**, 181 (1989).
- [81] G. R. Satchler, in *Isospin in Nuclear Physics*, edited by D. H. Wilkinson (North-Holland, Amsterdam, 1969), p. 389.
- [82] C. Barbieri and W. H. Dickhoff, *Phys. Rev. C* **63**, 034313 (2001).
- [83] C. Barbieri and W. H. Dickhoff, *Phys. Rev. C* **65**, 064313 (2002).
- [84] D. Schmitt and R. Santo, *Z. Phys.* **233**, 114 (1970).
- [85] P. Martin, B. Buenerd, Y. Dupont, and M. Chabre, *Nucl. Phys.* **A185**, 465 (1972).
- [86] M. E. Williams-Norton and R. Abegg, *Nucl. Phys.* **A291**, 429 (1977).
- [87] G. Audi, O. Bersillon, J. Blachot, and A. H. Wapstra, *Nucl. Phys.* **A624**, 1 (1997).